Nanosphere Lithography: Size-Tunable Silver Nanoparticle and Surface Cluster Arrays

John C. Hulteen,† David A. Treichel,‡ Matthew T. Smith, Michelle L. Duval, Traci R. Jensen, and Richard P. Van Duyne*

Department of Chemistry, Northwestern University, Evanston, Illinois 60208-3113

Received: February 9, 1999; In Final Form: March 24, 1999

Nanosphere lithography (NSL) is an inexpensive, inherently parallel, high-throughput, and materials-general nanofabrication technique capable of producing well-ordered 2D periodic particle arrays of nanoparticles. This paper focuses on the synthesis of size-tunable silver nanoparticle arrays by nanosphere lithography and their structural characterization by atomic force microscopy (AFM). The in-plane diameter, *a*, of Ag nanoparticles was tuned from 21 to 126 nm by systematic variation of the nanosphere diameter, *D*. Similarly, the out-of-plane height, *b*, was tuned from 4 to 47 nm by varying the mass thickness, d_m, of the Ag overlayer. Experimental measurements of *a*, *b*, and interparticle spacing d_{ip} of many individual nanoparticles as a function of *D* and d_m were carried out using AFM. These studies show (i) $b = d_m$, (ii) d_{ip} accurately corresponds to predictions based on the nanosphere mask geometry, (iii) *a*, after correction for AFM tip convolution, is governed only by the mask geometry and the standard deviation, σ_D, of the nanosphere diameter, and (iv) line-of-sight deposition is strictly operative. Furthermore, we have established that nanosphere lithography can fabricate nanoparticles that contain only ca. 4×10^4 atoms and are in the size range of a surface-confined cluster.

Introduction

Atomic clusters,[1−5] nanoparticles,[4,6−9] and nanostructures[10,11] of metals and semiconductors exhibit size-dependent properties that are profoundly different from the corresponding bulk material counterparts. Size-dependent properties of interest include, but are not limited to, the following: optical,[12−15] magnetic,[16,17] catalytic,[18−21] thermodynamic,[22,23] electrochemical,[24] and electrical transport.[8,25,26] Developing a fundamental understanding of these size-dependent properties and the factors that control them has been a primary motivation for this active area of cross-disciplinary research. An additional driving force has been the prospect of exploiting these size-dependent properties to create new functional materials and advanced devices. Resourceful use of the optical properties of nanoparticles has resulted in new types of filters,[27,28] substrates for surface-enhanced spectroscopies,[29−41] biosensors,[42−44] bioprobes,[45,46] chemical sensors,[47,48] and optical devices.[49−56] The magnetic properties of nanoparticles have applications to new data storage media[57,58] and biological probes.[59] New fundamental understanding of heterogeneous catalytic properties has arisen from the use of nanoparticle-based model systems.[18,19,21,60] Single-electron transistors have been developed based on the size-dependent electronic transport properties of nanoparticles.[61]

Two complementary approaches exist for the creation of nanostructured materials and the study of size-dependent properties. The first is the "bottom-up" approach, which is used primarily in gas-phase cluster beam studies[3,62] and condensed-phase colloid synthesis.[4,8] With these techniques, the size evolution of properties can be monitored from naked atomic clusters to particles and crystals having nanometer-sized dimensions. By use of the "bottom-up" strategy, much has been learned about the role of cluster structure, number of surface vs interior atoms, and quantum confinement effects in controlling the size-dependent properties. The second is the "top-down" approach, which uses advanced lithographic technologies to reduce the dimensions of bulk matter from the μm to the 10 nm regime. Several standard lithographic techniques are routinely used to create surface nanostructures with controlled size, shape, and spacing. These include photolithography, electron beam lithography (EBL),[63−65] X-ray lithography (XRL),[64,66,67] and ion beam lithography (IBL).[68] By far the most widely used is photolithography; however, it has not been widely applied to nanostructure fabrication as a consequence of its diffraction-limited resolution of ca. $\lambda/2$. The use of ultraviolet lasers,[69] holographic interferometry,[39−41,70] and high numerical aperture optics has significantly extended both its longevity and applicability to the sub-300 nm regime. While EBL, IBL, and XRL are eminently capable of producing a wide variety of nanostructures and may yet become the industrial-scale nanofabrication methodology of choice, they have inherent features that limit their applicability in many conventional laboratory situations. EBL is characterized by low sample throughput, high cost per nanostructure, and excellent minimum feature size combined with modest control of feature shape. For example, EBL has demonstrated 4 nm dots on 8 nm centers in a square lattice,[71,72] although 10 nm dots on 40 nm centers is probably a more practical limit.[57] IBL also has low sample throughput and high cost per nanostructure; however, it is additionally restricted to a space charge limited to a resolution of ca. 20 nm. Although XRL has an initially high capital cost, this is offset by its high throughput. Nevertheless, XRL experiences limitation due to problems with photoresist development, mask proximity, and a small feature size limit in the 20−30 nm range caused by photoelectron generation in the mask and diffraction effects.

* To whom correspondence should be addressed. E-mail: vanduyne@chem.nwu.edu.

† Present address: 3M Corporation, St. Paul, MN 55144.

‡ Present address: Department of Chemistry, Nebraska Wesleyan, Lincoln, NE 68504.

10.1021/jp9904771 CCC: $18.00
Published on Web 04/29/1999

In an attempt to circumvent both the limitations and inconveniences of the standard methods, there is substantial interest in developing new approaches to nanolithography that combine the resolution of EBL with the high throughput of XRL. Toward this goal, two basic strategies have been employed: (i) serial nanolithography based on scanning probe microscopy and (ii) parallel nanolithography based on phenomena with naturally occurring nanometer-scale periodicities. Scanning probe lithography based on AFM,[73−77] scanning tunneling microscopy (STM),[78−83] and scanning near-field optical microscopy (NSOM)[84,85] has been implemented, which is capable of manipulating individual atoms, molecules, and nanocrystals. Although scanning probe methodologies have demonstrated individual object control and excellent spatial resolution, the throughput of these methods is limited by their inherent serial processing speeds.[86]

To exploit the high-throughput advantage of parallel nanolithography, various phenomena with naturally occurring nanometer scale periodicities have been exploited. A particularly interesting example of occurring nanometer-scale periodicities is found in laser-focused atom deposition[87−90] and neutral atom lithography.[91] These techniques utilize the standing wave electric field patterns of high-resolution single-mode lasers, which can focus neutral or metastable atom beams to ca. 50−60 nm line widths for deposition or etching and therefore do not require the usually time-consuming step of making a mask in order to fabricate a nanostructure. Of course, the price of eliminating the mask is reduction in the ability to generate arbitrary patterns. Another important approach to maskless, parallel nanolithography is based on the principle of self-organized growth.[92−98] Self-organized growth has been observed in both metal[92,93,97] and semiconductor heteroepitaxy.[94,99,96,98] This method is having a significant impact on the important and difficult problem of fabricating quantum-dot lasers.[100] Nanoporous deposition masks, etch masks, and encapsulation media have been fabricated from electrochemically anodized aluminum,[101−105] nanochannel glass,[106−108] or polycarbonate track-etched membranes.[109, 110] In addition a particularly important class of nanoporous media involves the self-assembly of proteins[111] or polystyrene nanospheres[112−116] that form 2D crystals that function as deposition and etch masks. Deckman's pioneering work on the formation of 2D colloidal crystal masks consisting of a monolayer of nanospheres[112−116] has been used by others to fabricate quartz posts for Ag deposition and optical absorption studies,[117−119] quantum dot structures in GaAs-based semiconductors,[120−122] high-T_c Josephson effect devices,[123] and magnetic nanostructures.[124]

Previously, we have demonstrated that nanosphere lithography (NSL),[125] an operationally more descriptive term than the term natural lithography used by Deckman, has many desirable characteristics as a laboratory-scale nanofabrication tool. NSL is inexpensive (viz., less than $1 per sample), inherently parallel, high-throughput, and materials-general. Consequently, it is capable of producing well-ordered, 2D periodic arrays of nanoparticles from a wide variety of materials on many substrates. Our work has extended previous efforts in this area by establishing the existence of a second nanosphere mask geometry, the 2D colloidal crystal bilayer or double layer, and consequently a second pattern for periodic nanoparticle arrays. In addition we showed that AFM was a particularly powerful tool for the structural characterization of the periodic particle arrays produced from both single-layer and double-layer masks.

The purpose of this paper is to demonstrate that nanosphere lithography can be used for the quantitative nanofabrication of size-tunable periodic particle arrays simply by selecting an appropriate nanosphere diameter, D, and/or deposition mass thickness, d_m. The structural parameters derived from AFM measurements are compared to those predicted from a geometric model of the mask and the hypothesis that line-of-sight deposition is the only operative beam−mask−substrate interaction mechanism. The measured interparticle spacings, d_{ip}, agree exactly with those predicted from the model, and the out-of-plane heights, b, are found to be approximately equal to d_m with the greatest deviations occurring for very thin depositions. The unprocessed, experimentally measured values of the in-plane diameter, a, however, do not correspond as well with the model. Three factors contribute to the observed deviations: (1) AFM tip convolution; (2) annealing of sharply pointed features in the single-layer nanoparticles; (3) the in-plane particle shape derived from the geometric model, which is only an approximate representation of the true "as-deposited" shape. Application of a newly developed tip deconvolution procedure results in a greatly improved level of agreement between the predicted and measured values of the in-plane nanoparticle diameter. In addition, it is found that the distribution of a values is determined only by the standard deviation of the nanosphere diameter, σ_D. These results confirm the line-of-sight deposition hypothesis. Furthermore, we have established that nanosphere lithography can fabricate nanoparticles with $a = 21$ nm and $b = 4$ nm, which contain only ca. 4×10^4 atoms. Such nanoparticles are in the size range of surface-confined clusters. So far as we are aware, these are the first surface-confined cluster arrays ever synthesized by a parallel nanolithographic approach. Additionally, it should be pointed out that the small feature sizes available from nanosphere lithography approach those produced by the standard nanofabrication techniques (i.e., EBL, IBL, and XRL).

Experimental Section

Materials. Ag (99.99%, 0.50 mm diameter) was purchased from D. F. Goldsmith (Evanston, IL) and ruby red muscovite mica from Ashville-Schoonmaker Mica Co. (Newport News, VA). Tungsten vapor deposition boats were purchased from R. D. Mathis (Long Beach, CA).

Self-Assembly of Nanosphere Lithography Masks. The nanosphere lithography masks were created by spin-coating polystyrene nanospheres, Interfacial Dynamics Corporation (Portland, OR), onto the substrate of interest in a custom-built spin coater. Both 542 ± 7 and 401 ± 7 nm nanospheres were spin-coated at slow speed (viz., ∼300 rpm), while 264 ± 8 and 165 ± 3 nm nanospheres were spin-coated at high speed (viz., ∼3600 rpm). The physical dimensions of the substrate were chosen to be in the range 0.25−1.0 cm^2, and the entire substrate surface was spin-coated with nanospheres. The nanospheres were received from the manufacturer as a suspension in water and then further diluted in a solution of the surfactant Triton X-100/methanol (1:400 by volume) before spin-coating. The dilution factors for single-layer masks were ca. 1:1, 1:1, 1:3, and 1:6 (by volume) for the nanosphere sizes 542, 401, 264, and 165 nm, respectively. The surfactant was used to assist the solutions in wetting the substrate. Double-layer masks were self-assembled starting with the dilution factors for single-layer masks and empirically increasing the nanosphere concentration in the spin-coating solution to optimize the fraction of the surface covered by double-layer packing. The specimen-to-specimen reproducibility of single-layer nanosphere lithography masks is excellent with somewhat greater variability observed for double layers.

Physical Vapor Deposition of Ag Overlayer. Thin films of Ag were deposited in a modified Consolidated Vacuum

Corporation vapor deposition system[102] with a base pressure of 10^{-7} Torr. The mass thickness, d_m, and deposition rate, r_d, were measured for each film with a custom-built quartz crystal microbalance (QCM) calibrated by both linear sweep stripping voltammetry and STM.[38] Samples were mounted 240 mm above the effusive source with three 25 mm diameter apertures regularly spaced between the source and the sample to provide collimation of the physical vapor deposition beam. Furthermore, the samples were mounted such that the normal to the surface of the sample was parallel to the collimated physical vapor deposition beam. After deposition of Ag, polystyrene nanosphere "liftoff" from the mica substrate was achieved by dissolution in CH_2Cl_2 with the aid of sonication for 0.5−1 min.

AFM Measurements. All AFM images were collected either in air or in a N_2(g) environment on a Digital Instruments Nanoscope II microscope. Etched Si nanoprobe tips, Digital Instruments, with spring constants of approximately 0.15 N m^{-1} were used. These tips were conical in shape with a cone angle of 20° and an effective radius of curvature at the tip, $R_c = 10$ nm. The sharp features of these tips were necessary to reduce tip-induced image broadening and to decrease the effect of capillary forces with the surface. The images reported here are raw, unfiltered data collected in the constant-force mode with the applied force between 3 and 30 nN (under N_2(g) vs in air) and a scan speed of 8 lines s^{-1}. The scan head had a range of 12 μm × 12 μm.

Results and Discussion

Figure 1 schematically illustrates the packing arrangement of identical polymer nanospheres that forms the mask geometry, the resulting array of nanoparticles, and the large-area AFM images corresponding to single-layer and double-layer nanosphere lithography periodic particle arrays. Single-layer and double-layer periodic particle arrays were prepared using nanospheres with several different diameters, D = 542, 401, 264, and 165 nm. For each periodic particle array sample, the following structural parameters were measured by AFM: a, the nanoparticle's in-plane size; b, its out-of-plane height; d_{ip}, the center-to-center interparticle spacing. These experimentally derived structural parameters will be compared to those predicted from the structure of the nanosphere mask.

Structure of Single-Layer Periodic Particle Arrays. Single-layer periodic particle arrays are formed by the self-assembly of polymer nanospheres into a close-packed monolayer (Figure 1A) that acts as a material deposition mask. A gas-phase atom or molecular beam, formed by thermal evaporation in high vacuum, impinges on the mask. The material, which passes through the 3-fold, triangular-shaped interstices in the mask, is deposited on the substrate. Subsequent removal of the nanosphere mask by sonication and dissolution in CH_2Cl_2 results in a single-layer periodic particle array structure (Figure 1B). Figure 1C is a 5 μm × 5 μm AFM image of a single-layer periodic particle array showing zero defects. Clearly, nanosphere lithography is capable of fabricating single-layer periodic particle arrays with defect-free areas that are sufficiently large (viz., ∼ 25 μm^2) to probe the optical properties of Ag nanoparticles with far-field, UV−vis extinction microspectroscopy,[126] spatially resolved SERS,[127] or spatially registered AFM/SERS.[128] Figure 2A illustrates the geometric model used to define the in-plane structural parameters (viz., a_{SL} and $d_{ip,SL}$) describing nanoparticle shape and spacing for the single-layer periodic particle arrays.[125]

Figure 3 shows a series of AFM images and corresponding line scans for Ag nanoparticle arrays resulting from single-layer masks with decreasing nanosphere diameters, D = 542, 401, 264, and 165 nm, and constant Ag mass thickness, d_m = 18 nm. Table 1 summarizes the results of the single-layer nanoparticle structural parameters derived from line scans such as those pictured in Figure 3. For the case of D = 264 nm, a series of measurements at three different values of d_m = 40, 22, and 13 nm are included. To ensure that the data in Table 1 represents the global behavior of these single-layer arrays, at least 50 nanoparticles were measured at each of three different locations on the surface and their results averaged for each entry. The overall structural picture that emerges from the data in Figure 3 and Table 1 consists of four points: (1) the in-plane nanoparticle diameter, a_{SL}, can be systematically varied by selection of the nanosphere diameter, D; (2) the out-of-plane nanoparticle height, b_{SL}, can be continuously and independently tuned with respect to a_{SL} by variation of the mass thickness, d_m, of the Ag overlayer; (3) the interparticle spacing, $d_{ip,SL}$, can also be systematically varied by selection of the nanosphere diameter, D, but is, of course, linked to the value of a_{SL} through the mask geometry; (4) an in-plane nanoparticle shape transition from triangular (T) to elliptical (E) is observed with decreasing nanosphere size.

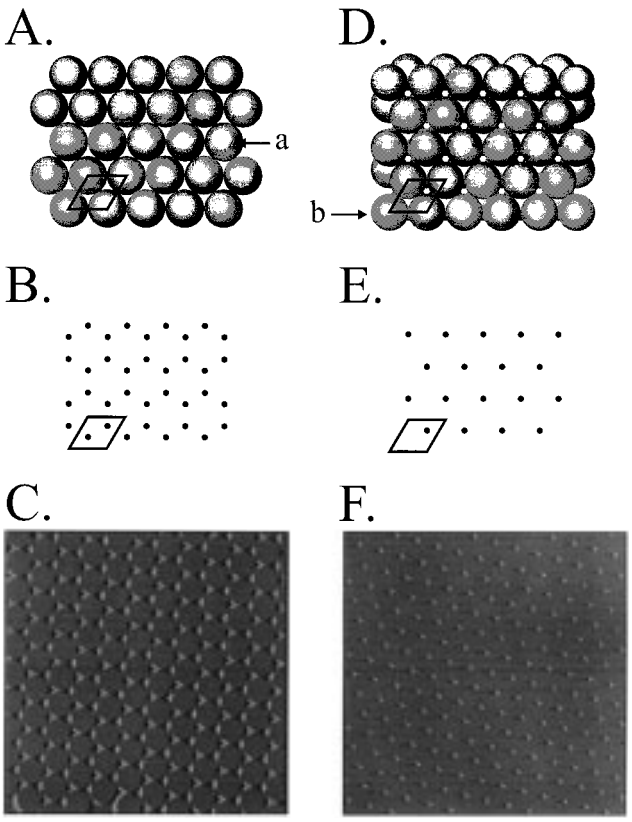

Figure 1. Schematic diagrams of single-layer (SL) and double-layer (DL) nanosphere masks and the corresponding periodic particle array (PPA) surfaces: (A) a(111) SL mask, dotted line = unit cell, a = first layer of hcp nanospheres; (B) SL PPA, two particles per unit cell; (C) 5 μm × 5 μm constant height AFM image of a Ag SL PPA on mica, D = 542 nm, d_m = 48 nm, r_d = 0.2 nm s^{-1}; (D) a(111)$p(1 \times 1)$-b DL mask, dotted line = unit cell, b = second layer of nanospheres; (E) DL PPA, one particle per unit cell; (F) 5.0 μm × 5.0 μm constant height AFM image of a DL PPA on mica, D = 400 nm, d_m = 30 nm, r_d = 0.2 nm s^{-1}.

A comparison of the experimental structural parameters with those predicted from the single-layer nanosphere mask geometry and the deposition conditions shows systematic deviations for a_{SL} but excellent agreement for b_{SL} and $d_{ip,SL}$. Three factors are believed responsible for the a_{SL} deviations: (1) AFM tip convolution; (2) surface melting of the sharp tips of these

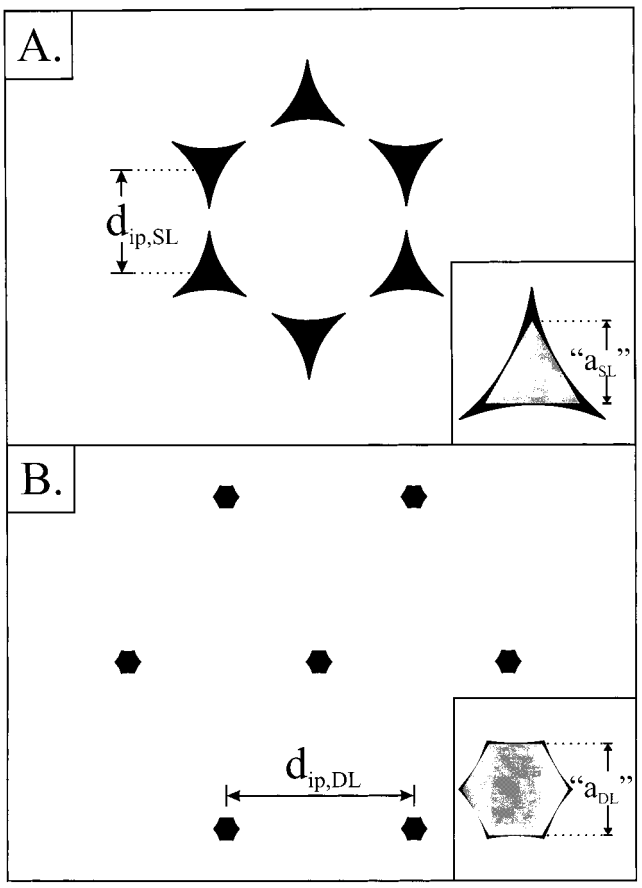

Figure 2. Projection of the holes created by (A) single-layer (SL) sphere mask and (B) double-layer (DL) sphere mask for a single unit cell. The insets of both (A) and (B) show a comparison of the predicted geometry (gray area) to that of the actual projection of the hole created by the sphere mask (black area). For the SL mask, the predicted particle geometry is the largest inscribed equilateral triangle, d_{ip} is defined as the interparticle spacing, and a is the in-plane particle diameter. From geometry, $d_{ip,SL}^{geom} = D/\sqrt{3} = 0.577D$ and a_{SL} is defined as the perpendicular bisector of the largest inscribed equilateral triangle, $a_{SL}^{geom} = (^3/_2)(\sqrt{3} - 1 - {}^1/_{\sqrt{3}})D = 0.233D$. For the DL mask, the predicted geometry is an inscribed regular hexagon. From geometry, the interparticle spacing is given by $d_{ip,DL}^{geom} = D$ and the in-plane particle diameter is given by $a_{DL}^{geom} = (\sqrt{3} - 1 - {}^1/_{\sqrt{3}})D = 0.155D$.

triangular nanoparticles; (3) the in-plane particle shape derived from the geometric model, which is only an approximate representation of the true "as-deposited" shape as shown in the inset of Figure 2A. A significant observation concerning a_{SL} (Table 1) is that its standard deviation is approximately equal to that of the nanosphere diameter distribution, σ_D. To demonstrate that this is, in fact, a more than causal relationship, a histogram representing the distribution of a_{SL} for the case where $D = 165$ nm and $d_m = 18$ nm is shown in Figure 4A. In addition a simulated Gaussian distribution with standard deviation, $\sigma_D = 3$ nm, equal to the nanosphere diameter distribution is superimposed on the histogram at $a_{SL} = 49$ nm (viz., the experimental average). It is clear that the experimental results lie entirely within the simulated Gaussian. Consequently, one can conclude that the measured distribution of a_{SL} is controlled by σ_D. We will return to the problem of measured vs predicted a_{SL} values below and show that by correcting for AFM tip convolution, the measurements can be brought into more satisfactory agreement with the geometric expectations. Table 1 also shows that the out-of-plane height of the single-layer nanoparticles agrees with d_m within 1−3 nm for the cases of $D = 542$, 401, and 264 nm. The exception is the case of $D = 165$ nm where $b_{SL} = 13 \pm 1$ nm is significantly less than the expected value $d_m = 18$ nm. A histogram depicting the distribution of b_{SL} for this case is shown in Figure 4B. No anomalies are observed such as a bimodal distribution. The origin of this discrepancy is not known. Finally, the experimental values of $d_{ip,SL}$ are found to be in excellent agreement with their geometrically predicted values. Here again, as in the data for a_{SL}, one finds that the experimental standard deviation of $d_{ip,SL}$ is approximately equal to σ_D. The histogram in Figure 4C demonstrates this and compares the experimental distribution of $d_{ip,SL}$ with that of a simulated Gaussian with standard deviation $\sigma_D = 3$ nm superimposed at $d_{ip,SL} = 95$ nm (the geometrically predicted value). The experimental results lie entirely within the simulated Gaussian, confirming that the measured distribution of $d_{ip,SL}$ is also controlled by σ_D. These observations concerning control of the structural precision of nanoparticles fabricated by nanosphere lithography are quite important to the practical fabrication of nanostructures for use in determining the size dependence of chemical and physical properties. Most commercial sources of nanospheres have $\sigma_D < 0.04D$. Thus, periodic particle arrays with similarly narrow structural parameter size distributions can be fabricated from readily available commercial materials. The precision of nanostructure fabrication by nanosphere lithography is at least comparable to if not better than that of electron beam lithography or other conventional nanofabrication approaches.

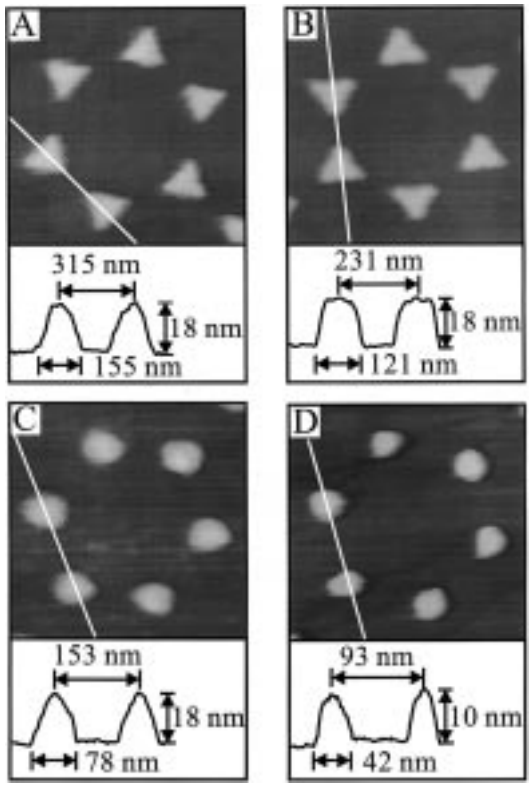

Figure 3. AFM images and line scans of Ag single-layer periodic particle arrays on mica substrates: (A) 870 nm × 870 nm image, $D = 542$ nm, $d_m = 18$ nm; (B) 610 nm × 610 nm image, $D = 401$ nm, $d_m = 18$ nm; (C) 420 nm × 420 nm image, $D = 264$ nm, $d_m = 18$ nm; (D) 260 nm × 260 nm image, $D = 165$ nm, $d_m = 14$ nm. All reported line scan values have not been deconvoluted for tip broadening effects.

Surface Melting in Single-Layer Ag Nanoparticle Arrays. In this section we consider the origin of the in-plane nanoparticle shape transition from triangular (T) to elliptical (E) with decreasing nanosphere size. Ag nanoparticles fabricated from the $D = 542$ nm and $D = 401$ nm single-layer masks are clearly triangular (Figure 3A and 3B). In contrast, one observes Ag

TABLE 1: Structural Parameters for Ag Nanoparticles Formed from Single Layer Masks

		prediction		experimental			corrected	cross
D (nm)[a]	d_m (nm)	d_{ip} (nm)	a (nm)	d_{ip} (nm)[b]	a (nm)[b]	b (nm)[b]	a (nm)	section[c]
542 ± 7	18	312 ± 7	126 ± 7	309 ± 9	153 ±6	18 ± 1	126	R
401 ± 7	18	231 ± 7	93 ± 7	229 ±10	121 ±6	19 ± 1	94	R
264 ± 8	40	152 ± 8	62 ± 8	152 ± 5	95 ± 4	37 ± 1	54	R
264 ± 8	22	152 ± 8	62 ± 8	152 ± 5	80 ± 3	23 ± 1	50	R
264 ± 8	13	152 ± 8	62 ± 8	152 ± 5	68 ± 4	14 ± 1	56	I, $\phi = 60°$
							53	H
165 ± 3	18	95 ± 3	38 ± 3	95 ± 2	49 ± 2	13 ± 1	37	I, $\phi = 60°$

[a] Standard deviations for nanosphere diameters were provided by the companies Bangs Laboratories and Interfacial Dynamics, Co. [b] Means and standard deviations for experimental data were derived from averaging particle height, size, and interparticle spacing for 50 measurements. [c] R = rectangular; I = isosceles trapezoid, ϕ = trapezoid base angle; H = hemiellipse.

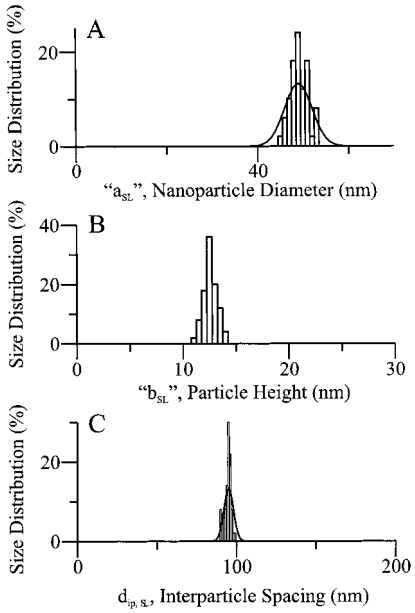

Figure 4. Histograms of the nanoparticle structural parameter distributions for a_{SL}, b_{SL}, and $d_{ip,SL}$ for a Ag single-layer periodic particle array on mica where $D = 165$ nm. The Gaussian in (A) is located at 49 nm, the average for the raw AFM data, and the Gaussian in (C) is located at 95 nm, the geometrically predicted value. Both Gaussians have a standard deviation equal to 3 nm.

nanoparticles with elliptical in-plane shapes when fabricated from $D = 264$ nm and $D = 165$ nm masks (Figure 3C and 3D). We postulate that this T → E shape transition, which occurs at or near room temperature, may be caused by size-dependent surface melting of Ag nanoparticles. The surface melting of platinum nanoparticles has recently been discussed by El-Sayed[23] in the context of the treatment by Buffat and Borel.[129] Application of this analysis to the case of a Ag nanoparticle suggests the plausibility of surface melting near room temperature. The ratio of the melting temperature T of a spherical Ag nanoparticle with radius r to that of bulk Ag, $T_0 = 962$ °C, is given by

$$\frac{T}{T_0} = 1 - \frac{2}{\rho_S \lambda}\left[\frac{\gamma_{SL}}{r - \delta}\right] \qquad (1)$$

where the density of the bulk solid, $\rho_S = 10\,490$ kg m^{-3}, is approximately equal to that of the bulk liquid and the heat of fusion, $\lambda = 105$ kJ kg^{-1}. If the tip regions of the triangular nanoparticles derived from $D = 264$ nm and $D = 165$ nm masks are taken to have radii of curvature, $r = 5$ nm, and a liquid layer thickness, $\delta = 0.25r$, then one calculates tip surface melting temperatures of $T = 471$, 28, and 0 °C for assumed values of $\gamma_{SL} = 1.0$, 2.0, and 3.0 N m^{-1}, respectively. Thus, surface melting of triangular nanoparticle tips is plausible given a sufficiently large γ_{SL}. Further support for the involvement of surface melting comes from a preliminary AFM structural study of Pt ($T_0 = 1769$ °C) nanoparticles.[130] In this study Pt nanoparticles were formed from single-layer masks with $D =$ 542, 401, 264, and 165 nm and constant Pt mass thickness, $d_m = 4$ nm (AFM images and corresponding line scans not shown). The single-layer Pt nanoparticles do not exhibit a T → E in-plane shape transition for $D \geq 165$ nm. This observation is consistent with the surface melting temperature $T > 500$ °C for 5 nm radius Pt nanoparticles reported previously.[23]

The calculation of the surface melting temperature of a Ag nanoparticle assumes that it is isolated and therefore neglects the interaction between the nanoparticle and its substrate surface. To examine the role of the nanoparticle−substrate interaction in a simple way, one may consider the surface tensions (viz., free energy per unit area) γ_0, γ_i, and γ_s corresponding to the Ag/vacuum (or ambient), Ag/substrate, and substrate/vacuum (or ambient) interfaces.[131] Under circumstances where $\gamma_0 + \gamma_i < \gamma_s$, Ag would wet the mica substrate, and one expects the triangular-shaped nanoparticle to "spread out" with an increase in a_{SL} accompanied by a decrease in b_{SL}. Similarly, if $\gamma_0 + \gamma_i > \gamma_s$, Ag would dewet the mica substrate, adopting a more compact shape with a decrease in a_{SL} and an increase in b_{SL}. The experimental data for the behavior of a_{SL} and b_{SL} as a function of D do not show either a systematic increase of a_{SL} accompanied by a decrease in b_{SL} or vice versa. Consequently, it is likely that surface melting rather than substrate wetting or dewetting is the dominant process determining the shape of single-layer Ag nanoparticles fabricated by nanosphere lithography.

Structure of Double-Layer Periodic Particle Arrays. A unique contribution of our work, which significantly extends the capabilities of nanosphere lithography, is the double-layer (DL) mask.[125] Double-layer nanosphere masks are formed by the self-assembly of more concentrated solutions of polymer nanospheres to form a 2D bilayer colloidal crystal (Figure 1D). The nanospheres of the second close-packed layer (B) lie in the depressions of the first layer (A). Formation of this AB close-packed structure occurs by a spontaneous, one-step process rather than sequential deposition of two nanosphere monolayers. As in the single-layer case, a gas-phase atom or molecular beam, formed by thermal evaporation in high vacuum, impinges on the mask. The material, which passes through the 6-fold hexagonal shaped interstices in the mask, is deposited on the substrate. Subsequent removal of the nanosphere mask by sonication and dissolution in CH_2Cl_2 results in the double-layer periodic particle array structure shown schematically in Figure 1E. Figure 1F is a 5 μm × 5 μm AFM image of a double-layer periodic particle array showing zero defects. Again, we point out that nanosphere lithography is capable of fabricating double-

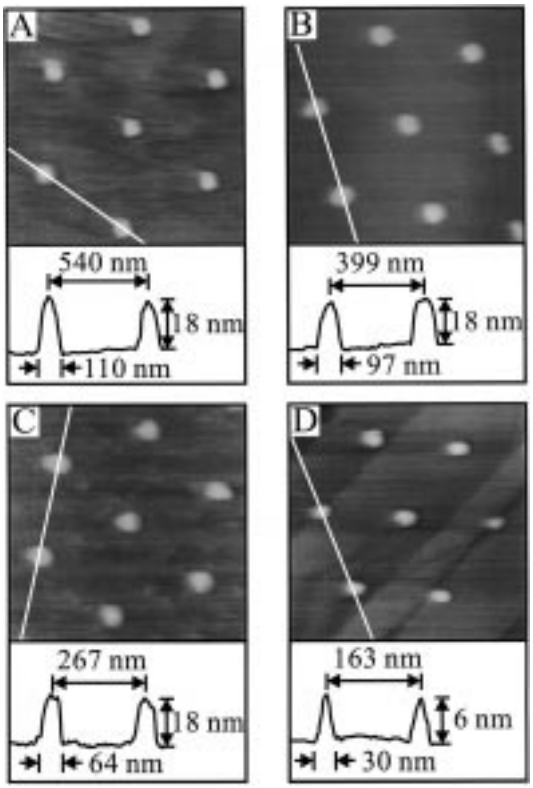

Figure 5. AFM images and line scans of Ag double-layer periodic particle arrays on mica substrates: (A) 1200 nm × 1200 nm image, D = 542 nm, d_m = 18 nm; (B) 1000 nm × 1000 nm image, D = 401 nm, d_m = 18 nm; (C) 670 nm × 670 nm image, D = 264 nm, d_m = 18 nm; (D) 410 nm × 410 nm image, D = 165 nm, d_m = 0.5 nm. Deposition and imaging conditions are identical to those in Figure 1.

layer periodic particle arrays with sufficiently large defect-free domains such that microspectroscopic probing of the optical properties is possible.[126−128] Figure 2A illustrates the geometric model used. Figure 2B illustrates the geometric model used to define the in-plane structural parameters (viz., a_{DL} and $d_{ip,DL}$) describing nanoparticle shape and interparticle spacing.[125]

Parts A−C of Figure 5 show a series of AFM images and corresponding line scans of Ag nanoparticle arrays resulting from double-layer masks with decreasing nanosphere diameters, D = 542, 401, 264, and a constant Ag mass thickness, d_m = 18 nm. Figure 5D shows the AFM image and line scan for the case of D = 165 nm and d_m = 0.5 nm, which represents our attempt to fabricate the smallest possible nanoparticles by nanosphere lithography. As a size reference, note that atomic step edges resulting from the cleavage of the mica substrate are clearly visible in this image. The nanoparticles in these double-layer arrays all have an in-plane elliptical shape and a uniform interparticle spacing. No in-plane shape transformations as a function of nanosphere size are observed. We will return to consider the properties of the smallest NSL nanoparticles in the section below on surface-confined clusters arrays. Table 2 summarizes the globally averaged results for the double-layer nanoparticle structural parameters derived from the line scans. At least 50 nanoparticles were measured at each of three different locations on the surface and their results averaged for each table entry. As with the corresponding single-layer studies, a_{DL} and $d_{ip,DL}$ are systematically varied by changing D while b_{DL} was varied through changes in d_m. The values of a_{DL} systematically deviate from their geometric predictions,[125] whereas, b_{DL} and $d_{ip,DL}$ are in excellent agreement. We will show that AFM tip convolution is responsible for the a_{DL} deviations. The distribution in the measurements of both a_{DL} and $d_{ip,DL}$ is again controlled entirely by σ_D as shown by the histograms and superimposed simulated Gaussian distributions in Figure 6A and 6C.

For the case of D = 264 nm, five nanoparticle arrays were fabricated with systematic variation of the Ag overlayer mass thickness. For the largest value of mass thickness studied, we found b_{DL} = 47 ± 2 nm, which is ca. 20% less than d_m = 60 nm. One might attempt to explain this deviation by invoking the hypothesis that $\gamma_0 + \gamma_i < \gamma_s$, which would lead to Ag wetting the mica substrate and the observed decrease in b_{DL}. This explanation falls short, since the concomitant increase in a_{DL} is not observed. In the intermediate mass thickness range, excellent agreement was found between b_{DL} and d_m = 40, 22, and 13 nm (Table 2). Finally, for the smallest value of mass thickness studied, d_m = 2 nm, we found that b_{DL} = 9 ± 1 nm, which is ca. 4 times greater than d_m = 2 nm. Here, the explanation is more likely to involve conditions where $\gamma_0 + \gamma_i > \gamma_s$, leading to Ag dewetting the mica substrate and the nanoparticle adopting a more compact shape accompanied by the observed increase in b_{DL}. The decrease in nanoparticle diameter expected to supply the material for the increase in nanoparticle height is, however, not observed. An alternative possibility is that the material required for increasing nanoparticle height is supplied by a decrease in the isosceles trapezoid base angle from ϕ = 60° to ∼45°. A change in base angle of this magnitude is, in fact, supported by AFM line scan data (not shown).

Correction of in-Plane Nanoparticle Size for AFM Tip Convolution. From examination of the experimental data reported for a_{SL} and a_{DL} in Tables 1 and 2, it is evident that the measured in-plane particle widths are systematically larger than the values predicted from the nanosphere mask geometries. Observations of in-plane feature size broadening are common in AFM studies and are attributed to the convolution of the real surface morphology with the tip shape function. Deconvolution methods to recover corrected feature sizes from experimental images have been discussed in the literature.[132−137] The deconvolution approach used here to recover corrected values for a_{SL} and a_{DL} is based on the ability to fabricate samples with continuously tunable out-of-plane heights b_{SL} and b_{DL}, which can be accurately determined from AFM line scan measurements. By convoluting a model AFM tip shape function with various assumed geometries for the out-of-plane nanoparticle cross section using corrected values of a as a free parameter, one can construct a family of working curves depicting the relationship between the observed in-plane nanoparticle diameter and out-of-plane height. The tip shape function, based on the manufacturer's specifications, was taken as a sphere with a radius of curvature R_c = 10 nm and a cone angle Θ = 20° (inset of Figure 7A). Working curves were computed for three out-of-plane nanoparticle cross section geometries: rectangular, hemielliptical, or isosceles trapezoidal. The working curve that passes through the most experimental data points is taken to simultaneously define the real in-plane diameter and the nanoparticle cross section shape.

Figure 7 illustrates the implementation of this correction procedure for the set of three Ag nanoparticle arrays formed from D = 264 nm single-layer masks with d_m = 40, 22, and 13 nm. Figure 7A shows only two members (for clarity) of a set of computed working curves depicting the functional relationship between in-plane nanoparticle diameter a_{SL} and out-of-plane nanoparticle height b_{SL} assuming that the nanoparticle cross section is rectangular. The upper working curve (solid line) assumes that the real in-plane nanoparticle diameter has the

TABLE 2: Structural Parameters for Ag Nanoparticles Formed from Double-Layer Masks

		predictions		experimental			corrected	cross
D (nm)[a]	d_m (nm)	d_{ip} (nm)	a (nm)	d_{ip} (nm)[b]	a (nm)[b]	b (nm)[b]	a (nm)	section[c]
542 ± 7	18	542 ± 7	84 ± 7	540 ± 9	111 ± 6	18 ± 1	84	R
401 ± 7	18	401 ± 7	62 ± 7	399 ± 7	97 ± 4	18 ± 1	70	R
264 ± 8	60	264 ± 8	41 ± 8	267 ± 7	94 ± 4	47 ± 2	46	R
264 ± 8	40	264 ± 8	41 ± 8	267 ± 7	88 ± 4	36 ± 2	48	R
264 ± 8	22	264 ± 8	41 ± 8	267 ± 7	75 ± 4	23 ± 1	45	R
264 ± 8	13	264 ± 8	41 ± 8	267 ± 7	55 ± 4	13 ± 1	43	I, $\phi = 60°$
264 ± 8	2	264 ± 8	41 ± 8	267 ± 7	49 ± 3	9 ± 1	41	I, $\phi = 45°$
165 ± 3	18	165 ± 3	26 ± 3	165 ± 3	41 ± 2	10 ± 1	28	I, $\phi = 30°$
165 ± 3	0.5	165 ± 3	26 ± 3	165 ± 3	27 ± 2	4 ± 1	21	I, $\phi = 30°$

[a] Standard deviations for nanosphere diameters were provided by the companies Bangs Laboratories and Interfacial Dynamics, Co. [b] Means and standard deviations for experimental data were derived from averaging particle height, size, and interparticle spacing for 50 measurements. [c] R = rectangular, I = isosceles trapezoid, ϕ = trapezoid base angle.

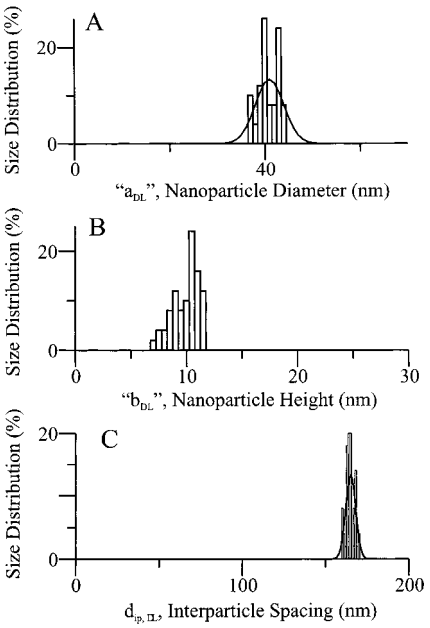

Figure 6. Histograms of the nanoparticle structural parameter distributions for a_{DL}, b_{DL}, and $d_{ip,DL}$ for a Ag double-layer periodic particle array on mica where $D = 165$ nm. The Gaussian in (A) is located at 41 nm, the average for the raw AFM data, and the Gaussian in (C) is located at 165 nm, the geometrically predicted value. Both Gaussians have a standard deviation equal to 3 nm.

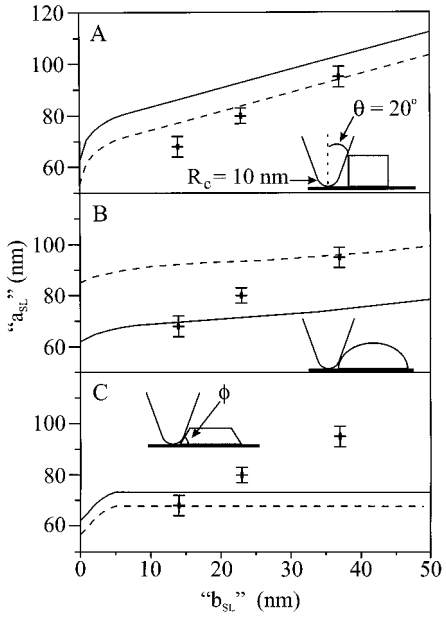

Figure 7. Tip single-layer nanoparticle convolution: plot of experimental a_{SL} vs b_{SL} (crosses with error bars) from Table 1 and various working curves modeling the dependence of a_{SL} vs b_{SL} for different assumed nanoparticle cross section geometries for the case of D = 264 nm. AFM tip parameters are radius of curvature $R_c = 10$ nm and cone angle $\phi = 20°$. (A) Rectangular prism nanoparticle cross section; (solid line) corrected value for $a_{SL} = 62$ nm; (dashed line) corrected value for $a_{SL} = 53$ nm. (B) Hemielliptical nanoparticle cross section; (solid line) corrected value for $a_{SL} = 62$ nm; (dashed line) corrected value for $a_{SL} = 83$ nm. (C) Isosceles trapezoidal nanoparticle cross section with base angle $\phi = 60°$; (solid line) corrected value for $a_{SL} = 62$ nm; (dashed line) corrected value for $a_{SL} = 56$ nm.

geometrically predicted value of $a_{SL} = 62$ n, whereas the lower working curve (dashed line) assumes the real value is $a_{SL} = 53$ nm. Figure 7B makes the assumption that the nanoparticle cross section is a hemiellipse and assumes that the real values of a_{SL} are 62 nm (solid line) and 83 nm (dashed line). Finally, in Figure 7C the nanoparticle cross section is assumed to be an isosceles trapezoid with base angle $\phi = 60°$ and the real values of a_{SL} are 62 nm (solid line) and 56 nm (dashed line). In all panels of Figure 7 the same three experimental values of a_{SL} and b_{SL} for the samples prepared with $d_m = 40$, 22, and 13 nm (Table 1) are superimposed on these curves as crosses with error bars. Examination of all three sets of working curves shows that no single assumption for the out-of-plane nanoparticle cross section accounts for all of the data. The "best" match between the computed working curves and the experimental points occurs for $b_{SL} > 20$ nm for the dashed line of Figure 7A and for $b_{SL} = 14$ nm for the dashed line of either Figure 7B or 7C. Combining this deconvolution analysis with the analysis of the in-plane T → E shape transition due to surface melting, one concludes that the Ag nanoparticles fabricated from single-layer $D = 264$ nm masks are best described as having elliptical in-plane cross sections (Figure 3C) and (1) rectangular out-of-plane cross sections for $d_m = 40$ and 22 nm, (2) hemielliptical or isosceles trapezoidal ($\phi \approx 60°$) out-of-plane cross sections for $d_m = 13$ nm, and (3) real in-plane diameters some 15−20% smaller than their geometrically predicted value of $a_{SL} = 62$ nm. Table 1 lists the results of similar deconvolution analyses applied to all the single-layer-derived Ag nanoparticles. In all cases best fits were found assuming a rectangular nanoparticle cross section when $b_{SL} > 20$ nm and a trapezoidal nanoparticle cross section when $b_{SL} < 20$ nm. It should be noted that the real in-plane diameters for the Ag nanoparticles fabricated from single-layer $D = 542$, 401, and 165 nm masks now exhibit excellent agreement at the level of a few nanometers with the geometric predictions.

In Figure 8 the AFM tip deconvolution procedure is applied to Ag nanoparticle arrays fabricated from $D = 264$ nm double-layer masks with $d_m = 60$, 40, 22, 13, and 2 nm. The same tip shape function described in Figure 7 is used. Figure 8A shows

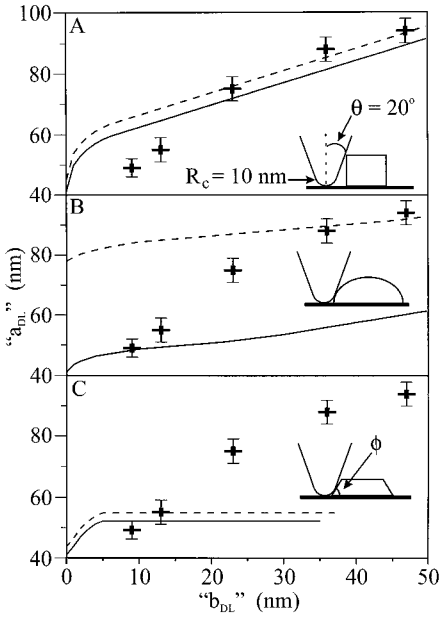

Figure 8. Tip double-layer nanoparticle convolution: plot of experimental a_{DL} vs b_{DL} (crosses with error bars) from Table 2 and various working curves modeling the dependence of a_{DL} vs b_{DL} for different assumed nanoparticle cross section geometries for the case of D = 264 nm. AFM tip parameters are radius of curvature $R_c = 10$ nm and cone angle $\theta = 20°$. (A) Rectangular prism nanoparticle cross section; (solid line) corrected value for $a_{DL} = 41$ nm; (dashed line) corrected value for $a_{DL} = 45$ nm. (B) Hemielliptical nanoparticle cross section; (solid line) corrected value for $a_{DL} = 41$ nm; (dashed line) corrected value for $a_{DL} = 78$ nm. (C) Isosceles trapezoidal nanoparticle cross section with base angle $\phi = 60°$; (solid line) corrected value for a_{DL} = 41 nm; (dashed line) corrected value for $a_{DL} = 43$ nm.

two members of a set of computed working curves for the dependence of in-plane nanoparticle diameter a_{DL} on out-of-plane nanoparticle height b_{DL} assuming that the out-of-plane nanoparticle cross section is rectangular. The upper curve takes the real value of a_{DL} as 45 nm (dashed line) and the lower curve the geometrically predicted value of $a_{DL} = 41$ nm (solid line). In Figure 8B the out-of-plane nanoparticle cross section is changed to that of a hemiellipse taking $a_{DL} = 78$ nm (dashed line) and $a_{DL} = 41$ nm (solid line) as the real values of in-plane nanoparticle diameter. Finally, in Figure 8C the out-of-plane nanoparticle cross section is assumed to be an isosceles trapezoid with $\phi = 60°$ and the real values of the in-plane diameter are $a_{DL} = 43$ nm (dashed line) and $a_{DL} = 41$ nm (solid line). In all panels of Figure 8, the same five experimental values of a_{DL} and b_{DL} for the samples prepared with different d_m = 60, 40, 22, 13, and 2 nm (Table 2) are superimposed on these curves as crosses with error bars. Examination of these working curves for the double-layer case indicates that, as in the single-layer case, no single assumption for the out-of-plane cross section accounts for all the data, implying the existence of an out-of-plane shape transition as a function of nanoparticle height. The "best" match between the computed working curves and the experimental points occurs for $b_{DL} > 20$ nm with the dashed line of Figure 8A and for $b_{DL} < 20$ nm with either the solid or dashed lines of Figure 8C. This deconvolution analysis indicates that the Ag nanoparticles fabricated from $D = 264$ nm double-layer masks are best described as having elliptical in-plane cross sections (Figure 5C) and (1) rectangular out-of-plane cross sections for d_m = 60, 40, 22 nm, (2) isosceles trapezoid out-of-plane cross sections for d_m = 13 and 2 nm, and (3) real in-plane diameters some 10−20% larger than their geometrically predicted value of $a_{DL} = 41$ nm. Table 2 lists the results of similar deconvolution analyses applied to all the double-layer-derived Ag nanoparticles. In all cases best fits were found assuming a rectangular nanoparticle cross section when $b_{DL} >$ 20 nm and a trapezoidal nanoparticle cross section when $b_{DL} <$ 20 nm. It should be noted that the real in-plane diameters for the Ag nanoparticles fabricated from double-layer D = 542, 401, and 165 nm masks now exhibit agreement at the level of ca. 10% with the geometric predictions.

Surface-Confined Cluster Arrays. The smallest Ag nanoparticles fabricated to date by nanosphere lithography are those derived from a $D = 165$ nm double-layer mask with $d_m = 0.5$ nm. They are similar to those shown in Figure 5D. The structural parameters for these nanoparticles as derived from AFM lines scans and the above tip deconvolution procedure are $a_{DL} = 21$ nm and $b_{DL} = 4 \pm 1$ nm with circular in-plane cross section and isosceles trapezoid ($\phi = 30°$) out-of-plane cross section. A nanoparticle with this structure and the bulk density of Ag is found to have a volume containing only ca. 4×10^4 atoms and a surface area containing ca. 5×10^3 atoms. Since metal clusters have been described as *particles composed of a countable number of atoms, starting with the diatomic molecule and reaching, with a vaguely defined upper band, several hundred thousand atoms*,[3] one can legitimately describe these arrays of nanoparticles fabricated from double-layer $D = 165$ nm masks with $d_m = 0.5$ nm as arrays of surface-confined clusters. As far as we are aware, this is the first example of surface cluster arrays fabricated by a parallel nanolithography. Although these Ag cluster arrays are somewhat larger than the Cu cluster arrays recently fabricated by Kolb[81] using electrochemical STM, one can anticipate that with further development nanosphere lithography may join the scanning probe nanolithography and nanoparticle manipulation methodologies as tools for the study of the material properties of surface-confined cluster arrays.

Conclusions

This paper has demonstrated that nanosphere lithography can be used to create periodic particle arrays using not only single-layer masks but double-layer polymer nanosphere masks. By exercising control over both D and d_m, we have shown the most systematic variation in nanoparticle size ever reported for nanosphere lithography. The nanoparticle structural parameters measured by AFM were in good agreement with the geometric predictions. Deviations from the geometric predictions can be attributed to imperfections in the geometric model and the shape of the nanoparticle cross section used in the tip deconvolution procedure. Also, the size distribution of the particle metrics is dictated entirely by the standard deviation of the nanosphere diameter used. The smallest of these particles has been proposed to contain only 4×10^4 Ag atoms, which could be classified as a surface periodic cluster array. Work is currently underway to use smaller nanospheres to obtain smaller periodic particle arrays, to use these masks to fabricate magnetic nanostructures, to measure experimental optical extinction spectra, and to model the optical extinction results using discrete dipole approximations.

Acknowledgment. The authors acknowledge the support of the National Science Foundation (CHE-940078), the MRSEC program of the National Science Foundation (DMR-9632472) at the Materials Research Center of Northwestern University, and ARO Grant DAAG55-97-1-0133.

References and Notes

(1) Benedek, G.; Martin, T. P.; Pacchioni, G. *Elemental and Molecular Clusters*; Springer Series in Materials Science; Springer-Verlag: Berlin, 1988; Vol. 6.

(2) Moskovits, M. *Annu. Rev. Phys. Chem.* **1991**, *42*, 465−499.
(3) de Heer, W. A. *Rev. Mod. Phys.* **1993**, *65*, 611−676.
(4) *Clusters and Colloids From Theory to Applications*; Schmid, G., Ed.; VCH Publishers: New York, Weinheim, 1994; p 555.
(5) Castleman, A. W.; Bowen, K. H. *J. Phys. Chem.* **1996**, *100*, 12911−12944.
(6) Steigerwald, M. L.; Brus, L. E. *Acc. Chem. Res.* **1990**, *23*, 183−188.
(7) Brus, L. E.; Trautman, J. K. *Philos. Trans. R. Soc. London A* **1995**, *353*, 313−321.
(8) Alivisatos, A. P. *J. Phys. Chem.* **1996**, *100*, 13226−13239.
(9) Alivisatos, A. P. *Science* **1996**, *271*, 933−937.
(10) Reed, M. A.; Kirk, W. P. *Nanostructures and Mesoscopic Systems*; Academic Press, Inc.: San Diego, 1991.
(11) Sundaram, M.; Chalmers, S. A.; Hopkins, P. F.; Gossard, A. C. *Science* **1991**, *254*, 1326−1335.
(12) Mulvaney, P. *Langmuir* **1996**, *12*, 788−800.
(13) Grabar, K. C.; Smith, P. C.; Musick, M. D.; Davis, J. A.; Walter, D. G.; Jackson, M. A.; Guthrie, A. P.; Natan, M. J. *J. Am. Chem. Soc.* **1996**, *118*, 1148−1153.
(14) Feldstein, M. J.; Keating, C. D.; Liau, Y.-H.; Natan, M. J.; Scherer, N. F. *J. Am. Chem. Soc.* **1997**, *119*, 6638−6647.
(15) Kreibig, U. Optics of Nanosized Metals. In *Handbook of Optical Properties. Optics of Small Particles, Interfaces, and Surfaces*; Hummel, R. E., Wissmann, P., Eds.; CRC Press: Boca Raton, FL, 1997; Vol. II, pp 145−190.
(16) New, R. M. H.; Pease, R. F. W.; White, R. L. *J. Vac. Sci. Technol. B* **1995**, *13*, 1089−1094.
(17) Shi, J.; Gider, S.; Babcock, K.; Awschalom, D. D. *Science* **1996**, *271*, 937−941.
(18) Bradley, J. S. The Chemistry of Transition Metal Colloids. In *Clusters and Colloids From Theory to Applications*; Schmid, G., Ed.; VCH Publishers: New York, Weinheim, 1994; pp 459−544.
(19) Street, S. C.; Xu, C.; Goodman, D. W. *Annu. Rev. Phys. Chem.* **1997**, *48*, 43−68.
(20) Heiz, U.; Vanolli, F.; Sanchez, A.; Schneider, W.-D. *J. Am. Chem. Soc.* **1998**, *120*, 9668−9671.
(21) Yang, M. X.; Gracias, D. H.; Jacobs, P. W.; Somorjai, G. A. *Langmuir* **1998**, *14*, 1458−1464.
(22) Volokitin, Y.; Sinzig, J.; de Jongh, L. J.; Schmid, G.; Vargaftik, M. N.; Moiseev, I. I. *Nature* **1996**, *384*, 621−623.
(23) Wang, Z. L.; Petroski, J. M.; Green, T. C.; El-Sayed, M. A. *J. Phys. Chem. B* **1998**, *102*, 6145−6151.
(24) Gorer, S.; Ganske, J. A.; Hemminger, J. C.; Penner, R. M. *J. Am. Chem. Soc.* **1998**, *130*, 9584−9593.
(25) Bezryadin, A.; Dekker: C.; Schmid, G. *Appl. Phys. Lett.* **1997**, *71*, 1273−1275.
(26) Andres, R. P.; Bielefeld, J. D.; Henderson, J. I.; Janes, D. B.; Kolagunta, V. R.; Kubiak, C. P.; Mahoney, W. J.; Osifchin, R. G. *Science* **1996**, *273*, 1690−1693.
(27) Flaugh, P. L.; O'Donnell, S. E.; Asher, S. A. *Appl. Spectrosc.* **1984**, *38*, 847−850.
(28) Munro, C. H.; Pajcini, V.; Asher, S. A. *Appl. Spectrosc.* **1997**, *51*, 1722−1729.
(29) Zou, S.; Williams, C. T.; Chen, E. K.-Y.; Weaver, M. J. *J. Am. Chem. Soc.* **1998**, *120*, 3811−3812.
(30) Emory, S. R.; Haskins, W. E.; Nie, S. *J. Am. Chem. Soc.* **1998**, *120*, 8009−8010.
(31) Emory, S. R.; Nie, S. *J. Phys. Chem. B* **1998**, *102*, 493−497.
(32) Kahl, M.; Voges, E.; Kostrewa, S.; Viets, C.; Hill, W. *Sens. Actuators*, in press.
(33) Zhu, J.; Xu, F.; Schofer, S. J.; Mirkin, C. A. *J. Am. Chem. Soc.* **1997**, *119*, 235−236.
(34) Pipino, A. C. R.; Schatz, G. C.; Van Duyne, R. P. *Phys. Rev. B* **1996**, *53*, 4162−4169.
(35) Yang, W. H.; Hulteen, J. C.; Schatz, G. C.; Van Duyne, R. P. *J. Chem. Phys.* **1996**, *104*, 4313−4323.
(36) Freeman, R. G.; Grabar, K. C.; Allison, K. J.; Bright, R. M.; Davis, J. A.; Guthrie, A. P.; Hommer, M. B.; Jackson, M. A.; Smith, P. C.; Walter, D. G.; Natan, M. J. *Science* **1995**, *267*, 1629−1632.
(37) Caldwell, W. B.; Chen, K.; Herr, B. R.; Mirkin, C. A.; Hulteen, J. C.; Van Duyne, R. P. *Langmuir* **1994**, *10*, 4109−4115.
(38) Van Duyne, R. P.; Hulteen, J. C.; Treichel, D. A. *J. Chem. Phys.* **1993**, *99*, 2101−2115.
(39) Liao, P. F.; Bergman, J. G.; Chemla, D. S.; Wokaun, A.; Melngailis, J.; Hawryluk, A. M.; Economou, N. P. *Chem. Phys. Lett.* **1981**, *81*, 355−359.
(40) Liao, P. F. Silver Structures Produced by Microlithography. In *Surface Enhanced Raman Scattering*; Chang, R. K., Furtak, T. E., Eds.; Plenum Press: New York, 1982; pp 379−390.
(41) Howard, R. E.; Liao, P. F.; Skocpol, W. J.; Jackel, L. D.; Craighead, H. G. *Science* **1983**, *221*, 117−121.
(42) Storhoff, J. J.; Elghanian, R.; Mucic, R. C.; Mirkin, C. A.; Letsinger, R. L. *J. Am. Chem. Soc.* **1998**, *120*, 1959−1964.
(43) Elghanian, R.; Storhoff, J. J.; Mucic, R. C.; Letsinger, R. L.; Mirkin, C. A. *Science* **1997**, *277*, 1078−1081.
(44) Mucic, R. C.; Storhoff, J. J.; Letsinger, R. L.; Mirkin, C. A. *Nature* **1996**, *382*, 607.
(45) Bruchez, M., Jr.; Moronne, M.; Gin, P.; Weiss, S.; Alivisatos, A. P. *Science* **1998**, *281*, 2013−2018.
(46) Chan, W. C. W.; Nie, S. *Science* **1998**, *281*, 2016−2018.
(47) Pan, G.; Kesavamoorthy, R.; Asher, S. A. *J. Am. Chem. Soc.* **1998**, *120*, 6525−6530.
(48) Weissman, J. M.; Sunkara, H. B.; Tse, A. S.; Asher, S. A. *Science* **1996**, *274*, 959−960.
(49) Asher, S.; Chang, S.-Y.; Tse, A.; Liu, L.; Pan, G.; Wu, Z.; Li, P. *Mater. Res. Soc. Symp. Proc.* **1995**, *374*, 305−310.
(50) Mansour, K.; Soileau, M. J.; Van Stryland, E. W. *J. Opt. Soc. Am. B* **1992**, *9*, 1100−1109.
(51) Woileau, M. J. *Proceedings of SPIE—The International Society for Optical Engineering. Materials for Optical Switches, Isolators, and Limiters*; SPIE: Washington, 1989; Vol. 1105.
(52) Lidorikis, E.; Li, Q.; Soukoulis, C. M. *Phys. Rev. E* **1997**, *55*, 3613−3618.
(53) Neuendorf, R.; Quinten, M.; Kreibig, U. *J. Chem. Phys.* **1996**, *104*, 6348−6354.
(54) Schubert, E. F.; Hunt, N. E. J.; Micovic, M.; Malik, R. J.; Sivco, D. L.; Cho, A. Y.; Zydzik, G. J. *Science* **1994**, *265*, 943−945.
(55) Wanke, M. C.; Lehmann, O.; Müller, K.; Wen, Q.; Stuke, M. *Science* **1997**, *275*, 1284−1286.
(56) Joannopoulos, J. D.; Villeneuve, P. R.; Fan, S. *Nature* **1997**, *386*, 143−149.
(57) Chou, S. Y.; Krauss, P. R.; Zhang, W.; Guo, L.; Zhuang, L. *J. Vac. Sci. Technol. B* **1997**, *15*, 2897−2904.
(58) Chou, S. Y. *Proc. IEEE* **1997**, *85*, 652−671.
(59) Baselt, D. R.; Lee, G. U.; Hansen, K. M.; Chrisey, L. A.; Colton, R. J. *Proc. IEEE* **1997**, *85*, 672−680.
(60) Valden, M.; Lai, X.; Goodman, D. W. *Science* **1998**, *281*, 1647−1650.
(61) Kurihara, K.; Namatsu, H.; Nagase, M.; Makino, T. *Microelectron. Eng.* **1997**, *35*, 261−264.
(62) Halperin, W. P. *Rev. Mod. Phys.* **1986**, *58*, 533−606.
(63) Pease, R. F. W. *J. Vac. Sci. Technol. B* **1992**, *10*, 278−285.
(64) Pease, R. F. Patterning Techniques for sub-100 nm Devices, Circuits and Systems. In *Nanostructures and Mesoscopic Systems*; Kirk, W. P., Reed, M. A., Eds.; Academic Press: Boston, 1992; pp 37−50.
(65) McCord, M. A. *J. Vac. Sci. Technol. B* **1997**, *15*, 2125−2129.
(66) Smith, H. I.; Schattenburg, M. L. *IBM J. Res. Dev.* **1993**, *37*, 319−329.
(67) Silverman, J. P. *J. Vac. Sci. Technol. B* **1997**, *15*, 2117−2124.
(68) Melngailis, J.; Mondelli, A. A.; Berry, I. L., III; Mohondro, R. *J. Vac. Sci. Technol. B* **1998**, *16*, 927−957.
(69) Bloomstein, T. M.; Horn, M. W.; Rothschild, M.; Kunz, R. R.; Palmacci, S. T.; Goodman, R. B. *J. Vac. Sci. Technol. B* **1997**, *15*, 2112−2116.
(70) Kitson, S. C.; Barnes, W. L.; Sambles, J. R. *IEEE Photonics Technol. Lett.* **1996**, *8*, 1662−1664.
(71) Craighead, H. G.; Mankiewich, P. M. *J. Appl. Phys.* **1982**, *53*, 7186−7188.
(72) Craighead, H. G. ∼10 nm Electron-Beam Lithography with an (S)-TEM. In *Microbeam Analysis*; Romig, A. G., Jr., Goldstein, J. I., Eds.; San Francisco Press: San Francisco, 1984; pp 73−75.
(73) Manne, S.; Hansma, P. K.; Massie, J.; Elings, V. B.; Gewirth, A. A. *Science* **1991**, *251*, 183−186.
(74) Muller, W. T.; Klein, D. L.; Lee, T.; Clarke, J.; McEuen, P. L.; Schultz, P. G. *Science* **1995**, *268*, 272−273.
(75) Juno, T.; Carsson, S.-B.; Xu, H.; Montelius, L.; Samuelson, L. *Appl. Phys. Lett.* **1998**, *72*, 548−550.
(76) Martin, M.; Roschier, L.; Hakonen, P.; Parts, U.; Paalanen, M.; Schleicher, B.; Kauppinen, E. I. *Appl. Phys. Lett.* **1998**, *73*, 1505−1507.
(77) Resch, R.; Bugacov, A.; Baur, C.; Koel, B. E.; Madhukar, A.; Requicha, A. A. G.; Will, P. *Appl. Phys. A* **1998**, *67*, 265−271.
(78) Eigler, D. M.; Schweizer, E. K. *Nature* **1990**, *344*, 524−526.
(79) Stroscio, J. A.; Eigler, D. M. *Science* **1991**, *254*, 1319−1326.
(80) Schoer, J. K.; Crooks, R. M. *Langmuir* **1997**, *13*, 2323−2332.
(81) Kolb, D. M.; Ullmann, R.; Will, T. *Science* **1997**, *275*, 1097−1099.
(82) Meyer, G.; Rieder, K. H. *Mater. Res. Soc. Bull.* **1998**, 28−32.
(83) Chey, S. J.; Huang, L.; Weaver, J. H. *Appl. Phys. Lett.* **1998**, *72*, 2698−2700.
(84) Aizenberg, J.; Rogers, J. A.; Paul, K. E.; Whitesides, G. M. *Appl. Phys. Lett.* **1997**, *71*, 3773−3775.
(85) Madsen, S.; Bozhevolnyi, S. I.; Birkelund, K.; Müllenborn, M.; Hvam, J. M.; Grey, F. *J. Appl. Phys.* **1997**, *82*, 49−53.

(86) Dagata, J. A.; Marrian, C. R. K. *Technology of Proximal Probe Lithography*; SPIE Optical Engineering Press: Bellingham, Washington, 1993; Vol. 10.
(87) Timp, G.; Behringer, R. E.; Tennant, D. M.; Cunningham, J. E.; Pretiss, M.; Berggren, K. K. *Phys. Rev. Lett.* **1992**, *69*, 1636−1639.
(88) McClelland, J. J.; Scholten, R. E.; Palm, E. C.; Celotta, R. J. *Science* **1993**, *262*, 877−880.
(89) Scholten, R. E.; McClelland, J. J.; Palm, E. C.; Gavrin, A.; Celotta, R. J. *J. Vac. Sci. Technol. B* **1994**, *12*, 1847−1850.
(90) Celotta, R. J.; Gupta, R.; Scholten, R. E.; McClelland, J. J. *J. Appl. Phys.* **1996**, *79*, 6079−6083.
(91) Thywissen, J. H.; Johnson, K. S.; Dekker, N. H.; Prentiss, M.; Wong, S. S.; Weiss, K.; Grunze, M. *J. Vac. Sci. Technol. B* **1998**, *16*, 1155−1160.
(92) Chambliss, D. D.; Wilson, R. J.; Chiang, S. *Phys. Rev. Lett.* **1991**, *66*, 1721−1724.
(93) Roder, H.; Hahn, E.; Brune, H.; Bucher, J.-P.; Kern, K. *Nature* **1993**, *366*, 141−143.
(94) Nötzel, R.; Temmyo, J.; Tamamura, T. *Nature* **1994**, *369*, 131−133.
(95) Murray, C. B.; Kagan, C. R.; Bawendi, M. G. *Science* **1995**, *270*, 1335−1338.
(96) Tersoff, J.; Teichert, C.; Lagally, M. G. *Phys. Rev. Lett.* **1996**, *76*, 1675−1678.
(97) Bromann, K.; Felix, C.; Brune, H.; Harbich, W.; Monot, R.; Buttet, J.; Kern, K. *Science* **1996**, *274*, 956−958.
(98) Springholz, G.; Holy, V.; Pinczolits, M.; Bauer, G. *Science* **1998**, *282*, 734−737.
(99) Xie, Q.; Madhukar, A.; Chen, P.; Kobayashi, N. P. *Phys. Rev. Lett.* **1995**, *75*, 2542−2545.
(100) Fasol, G. *Science* **1997**, *275*, 941−942.
(101) Foss, C. A., Jr.; Hornyak, G. L.; Stockert, J. A.; Martin, C. R. *J. Phys. Chem.* **1994**, *98*, 2963−2971.
(102) Martin, C. R. *Science* **1994**, *266*, 1961−1966.
(103) Routevitch, D.; Bibioni, T.; Moskovits, M.; Xu, J. M. *J. Phys. Chem.* **1996**, *100*, 14037−14047.
(104) Hornyak, G. L.; Patrissi, C. J.; Martin, C. R. *J. Phys. Chem. B* **1997**, *101*, 1548−1555.
(105) Hulteen, J. C.; Patrissi, C. J.; Miner, D. L.; Crosthwait, E. R.; Oberhauser, E. B.; Martin, C. R. *J. Phys. Chem. B* **1997**, *101*, 7727−7731.
(106) Tonucci, R. J.; Justus, B. L.; Campillo, A. J.; Ford, C. E. *Science* **1992**, *258*, 783−785.
(107) Pearson, D. H.; Tonucci, R. J. *Science* **1995**, *270*, 68−70.
(108) Nguyen, P. P.; Pearson, D. H.; Tonucci, R. J. *J. Electrochem. Soc.* **1998**, *145*, 247−251.
(109) Whitney, T. M.; Jiang, J. S.; Searson, P. C.; Chien, C. L. *Science* **1993**, *261*, 1316−1319.
(110) Schönenberger, C.; van der Zande, B. M. I.; Fokkink, L. G. J.; Henny, M.; Schmid, C.; Krüger, M.; Bachtold, A.; Huber, R.; Birk, H.; Staufer, U. *J. Phys. Chem. B* **1997**, *101*, 5497−5505.
(111) Douglas, K.; Devaud, G.; Clark, N. A. *Science* **1992**, *257*, 642−644.
(112) Deckman, H. W.; Dunsmuir, J. H. *Appl. Phys. Lett.* **1982**, *41*, 377−379.
(113) Deckman, H. W.; Dunsmuir, J. H. *J. Vac. Sci. Technol. B* **1983**, *1*, 1109−1112.
(114) Roxlo, C. B.; Deckman, H. W.; Ables, B. *Phys. Rev. Lett.* **1986**, *57*, 2462−2465.
(115) Deckman, H. W.; Moustakas, T. D. *J. Vac. Sci. Technol. B* **1988**, *6*, 316−318.
(116) Deckman, H. W.; Dunsmuir, J. H.; Garoff, S.; McHenry, J. A.; Peiffer, D. G. *J. Vac. Sci. Technol. B* **1988**, *6*, 333−336.
(117) Russell, B. K.; Mantovani, J. G.; Anderson, V. E.; Warmack, R. J.; Ferrell, T. L. *Phys. Rev. B* **1987**, *35*, 2151−2154.
(118) Buncick, M. C.; Warmack, R. J.; Ferrell, T. L. *J. Opt. Soc. Am. B* **1987**, *4*, 927−933.
(119) Wachter, E. A.; Moore, A.; Haas, J. W., III. *Vib. Spectrosc.* **1992**, *3*, 73−78.
(120) Fang, H.; Zeller, R.; Stiles, P. J. *Appl. Phys. Lett.* **1989**, *55*, 1433−1435.
(121) Iwabuchi, T.; Chuang, C.; Khitrova, G.; Warren, M. E.; Chavez-Pirson, A.; Gibbs, H. M.; Sarid, D.; Gallagher, M. *SPIE* **1990**, *1284*, 142−148.
(122) Green, M.; Garcia-Parajo, M.; Khaleque, F. *Appl. Phys. Lett.* **1993**, *62*, 264−266.
(123) Dozier, W. D.; Daly, K. P.; Hu, R.; Platt, C. E.; Wire, M. S. *IEEE Trans. Magn.* **1990**, *27*, 3223−3226.
(124) Wiesendanger, R.; Bode, M.; Kleiber, M.; Lahndorf, M.; Pascal, R.; Wadas, A. *J. Vac. Sci. Technol. B* **1997**, *15*, 1330−1334.
(125) Hulteen, J. C.; Van Duyne, R. P. *J. Vac. Sci. Technol. A* **1995**, *13*, 1553−1558.
(126) Craighead, H. G.; Niklasson, G. A. *Appl. Phys. Lett.* **1984**, *44*, 1134−1136.
(127) Van Duyne, R. P.; Haller, K. L.; Altkorn, R. I. *Chem. Phys. Lett.* **1986**, *126*, 190−196.
(128) Smith, M. T.; Jensen, T. R.; Lackowski, W. M.; Van Duyne, R. P. *J. Phys. Chem. B*, in press.
(129) Buffat, P.; Borel, J.-P. *Phys. Rev. A* **1976**, *13*, 2287−2297.
(130) Lackowski, W. M. Interactions between Surfaces and Photons: Combination of Surface Enhanced Raman Spectroscopy with Atomic Force Microscopy and Pulsed Laser Deposition of III−V Semiconductors. Ph.D. Thesis, Northwestern University, 1998.
(131) Zangwill, A. *Physics at Surfaces*; Cambridge University Press: Cambridge, 1988.
(132) Li, Y.; Lindsay, S. M. *Rev. Sci. Instrum.* **1991**, *61*, 2630−2633.
(133) Keller, D. *Surf. Sci.* **1991**, *253*, 353−364.
(134) Bustamante, C.; Vesenka, J.; Tang, C. L.; Rees, W.; Guthold, M.; Keller, R. *Biochemistry* **1992**, *31*, 22−26.
(135) Vesenka, J.; Hansma, H.; Siegerist, C.; Siligardi, G.; Schabtach, E.; Bustamante, C. *SPIE* **1992**, *1639*, 127−137.
(136) Hutter, J. L.; Bechhoefer, J. *Rev. Sci. Instrum.* **1993**, *64*, 1868−1873.
(137) Markiewicz, P.; Goh, M. C. *Langmuir* **1994**, *10*, 5−7.